Rotational dynamics of a soft filament: Wrapping transition and propulsive forces

Naïs Coq, Olivia Du Roure, Joël Marthelot, Denis Bartolo, Marc Fermigier

Rotational dynamics of a soft filament: wrapping transition and propulsive forces

N. Coq, O. du Roure, J. Marthelot, D. Bartolo & M. Fermigier
Laboratoire de Physique et Mécanique des Milieux Hétérogènes,
ESPCI-CNRS UMR7636-Paris 6-Paris 7, 10 rue Vauquelin, 75005 Paris, France
(Dated: February 12, 2008)

We analyze experimentally the shape of a long elastic filament rotating in a viscous liquid. We identify a continuous but sharp transition from a straight to an helical shape, resulting from the competition between viscous stresses and elastic forces. This induced helicity generates a propulsive force along the axis of rotation. In addition, we show that the shape transition is associated with an unstable branch in the force-torque relation, confirming the numerical predictions of Manghi *et al.* [13]. A linearized model of the fluid-structure interaction is proposed to account for all the features of the non-linear filament dynamics.

Many cells use the beating of elastic filaments to swim or to pump fluids [1]. Prominent examples are the swimming of sperm cells which propel themselves by exciting propagative deformations along a single flagellum [2], and the pumping of liquid by the helical motion of cilia on embryo nodal cells [3]. Since the pioneering work of Taylor in the early 50s, the observation of these fascinating biological machines has inspired numerous studies on the fluid-structure interaction of flexible filaments with viscous flows. Moreover, recent advances in the construction of complex colloidal assembly [4, 5] and in the coupling of biological machines to artificial microstructures [7] should allow man-made swimmers to catch up with microorganisms. A promising example has already been proposed by Dreyfus *et.al.* who have quantitavely studied the propulsion of the first artificial flexible microswimmer [6]. So far, special attention has been paid to the thrust produced by the periodic and planar oscillations of an isolated flagella [6, 8, 9, 10, 11, 12]. However, in the last two years, a set of numerical and theoretical works [13, 14] has been devoted to another propulsion mechanism, the rotation of a single tilted flexible rod.

In this paper we present an experimental realization of this system. We show that, increasing the angular velocity, ω, the filament undergoes a sharp but continuous shape transition from a linear to an helical shape tightly wrapped around the rotation axis. We show that this collapse of the flexible rod is solely ruled by the interplay between the elastic forces and the viscous drag acting on it. The relation between the filament shape, the axial force and the rotation torque acting on the filament is investigated using a high resolution imaging method and described quantitatively thanks to a simple model of the fluid-structure interaction. We also give experimental evidence that a torque-controlled rotation should lead to strongly non linear and unstable filament dynamics [13].

We rotate a flexible filament immersed in a transparent plexiglas tank (dimensions 20 x 20 x 20 cm^3) filled with pure glycerin. The shear viscosity, η, of the glycerin has been systematically measured prior to each experiment. We did not measure any change due to possible temperature or hygroscopic variations: $\eta = 1\,\mathrm{Pa.s}$. The filaments are made of a low modulus polyvinylsiloxane elastomer. Glass capillary tubes are filled with a mixture of polymer and curing agent containing dispersed iron carbonyl particles intended to match the density of glycerin. Once the polymer is cured the glass capillary is broken to recover a cylindrical elastic rod of radius $a = 435\,\mu$m, which length varies from 2 cm to 10 cm. The Young's modulus $E = 0.7$ MPA of each rod was measured by dynamical mechanical analysis. The filaments are then attached to the axis of an electric motor delivering a discrete set of rotation speeds ranging from 0.01 to 10 rpm through a gear box. In all our experiments, the motor axis and the filament at rest make an angle θ of 15°. We simultaneously take pictures of the rotating filaments in two perpendicular directions with a 6 MPixels digital camera (Nikon D70). Eventually, we use a correlation algorithm

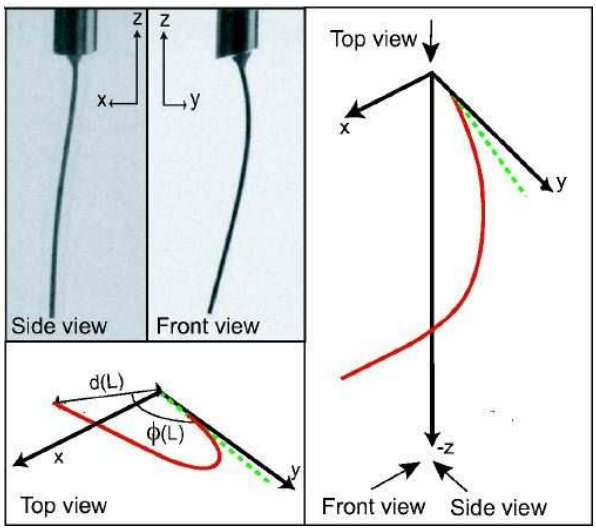

FIG. 1: Top left: front and side view of a rotating filament. Right: reconstructed 3D shape of the filament (solid line) and slope at the anchoring point (dashed line). Bottom left: projection of the filament shape in the (x, y) plane perpendicular to the rotation axis (solid line) and slope at the anchoring point (dashed line).

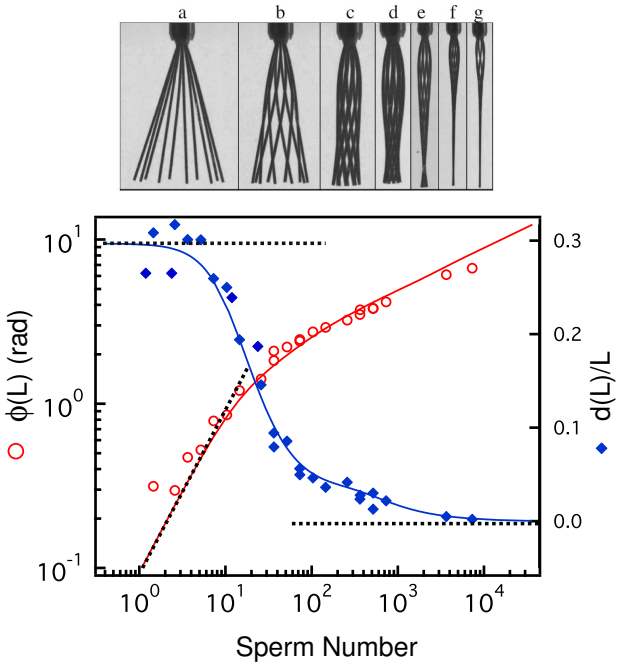

FIG. 2: Polar angle in the (x, y) plane (circles) and distance to the axis (diamonds) of the free end of the filament as a function of the dimensionless angular velocity Sp. Solid lines are solutions of the linearized deformation equation. Dashed lines: analytical solution in the low and high Sp limits, see main text. On top, corresponding shapes of the rotating filament (superimposed pictures at different times within a period).

to detect the coordinates of the two corresponding projected profiles, which allows for the determination of the full 3D shape of the distorted rods with a submillimeter accuracy, Figure 1. After a transient regime the rotating filament reaches a stationary shape and undergoes a rigid body rotation. The shortest rods are hardly deformed by the viscous flow even when the rotation speed is increased by 3 orders of magnitude. They rapidly adopt a slightly chiral shape close to the initial straight and tilted conformation. The rods with intermediate lengths display a continuous but sharp transition from an almost straight to an helical shape when increasing the angular velocity, figure 2. The longest rods are significantly bent by the viscous drag; after a long transient regime ($\sim$ 1 hour), they are tightly wrapped around the rotation axis even at the slowest rotation speed. In all that follows, we restrain our attention only to the final stationary shapes.

To go beyond the above qualitative observations, the dimensionless distance to the rotation axis, $d(L)/L$ and the polar angle $\phi(L)$ of the rod end are plotted in figure 2 as a function of the non dimensional rotation speed $\mathrm{Sp} \equiv \omega\eta_\perp L^4/\kappa$. Sp is commonly referred to as the sperm number, it compares the period of angular rotation to the

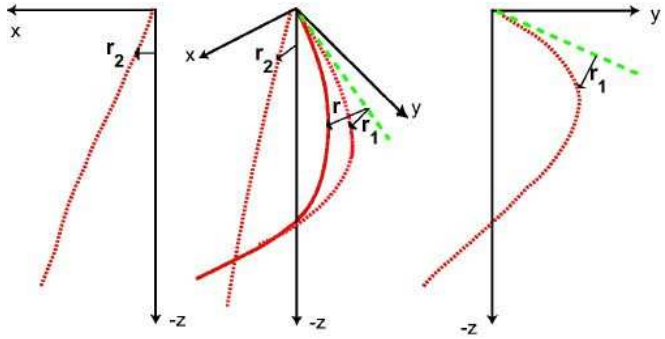

FIG. 3: Sketch of the filament deformations in the (x,z) and (y,z) planes illustrating the definition of the displacement field $\mathbf{r}(s) = (r_1(s), r_2(s))$. Solid lines: filament shape in 3D. Dashed lines: undeformed filament. Dotted lines: projections of the filament on the (x,z) and (y,z) planes.

elasto-viscous relaxation time, $\tau = \eta_\perp L^4/\kappa$, of the bending mode of wavelength L [9, 15], where $\kappa = \pi E a^4/4$ is the bending modulus of the filament and $\eta_\perp$ is the drag coefficient for normal motion. First of all, it is worth noticing that all the experimental data collapse on the same master curve, which implies that the deformation of the rods results from the competition between viscous and elastic forces.

At low Sp, the polar angle $\phi(L)$ increases linearly with ω whereas $d(L)/L$ remains constant over more than two decades. Above $Sp \approx 10$, the variation of the polar angle becomes much weaker. Conversely, the distance to the rotation axis drops down to a very small value. Surprisingly, a quantitative description of this wrapping transition can be performed ignoring both geometrical nonlinearities and long-range hydrodynamic coupling. To determine the filament shape we compute the elastic and the viscous forces acting on the flexible rod. Using a local drag description the viscous force is

$$\mathbf{f}_\mathrm{v} = (\eta_\parallel - \eta_\perp)(\mathbf{t}.\mathbf{v})\mathbf{t} + \eta_\perp \mathbf{v}, \qquad (1)$$

with $\mathbf{t}$ the tangent vector, $\eta_\perp = 4\pi\eta/\left[\log(L/a) + \frac{1}{2}\right]$ and $\eta_\parallel = 2\pi\eta/\left[\log(L/a) - \frac{1}{2}\right]$ the drag coefficients in the slender body approximation [16]. The elastic force $\mathbf{f_e}$ derives from the bending energy functional written within the small deformations approximation $\mathcal{E} = \frac{1}{2}\int \kappa(\partial_s^2\mathbf{r})^2\,\mathrm{d}s$, with s the curvilinear coordinate. $\mathbf{r}(s) = (r_1(s), r_2(s))$ is the displacement field normal to the undeformed filament, see Figure 3. Ignoring the incompressibility constraint which would only add extra nonlinear contributions to the linearized elastic force: $\mathbf{f}_\mathrm{e} = -\kappa\partial_s^4\mathbf{r}$, the filament shape can then be exactly computed by solving the force balance equation $\mathbf{f}_\mathrm{e} = -\mathbf{f}_\mathrm{v}$ in the frame rotating at ω around the z axis. Introducing the penetration length of the bending modes

$l(\omega) \equiv [\kappa/(\eta_\perp \omega \cos\theta)]^{1/4}$ this equation can be written in the compact form:

$$l^4(\omega)\partial_s^4 r_1 = -r_2 - s\tan\theta, \quad (2)$$
$$l^4(\omega)\partial_s^4 r_2 = r_1. \quad (3)$$

with the torque and force free conditions at $s = L$: $\partial_s^2\mathbf{r}(L) = \partial_s^3\mathbf{r}(L) = 0$ and the geometrical constraints on the rotation axis: $\mathbf{r}(0) = \partial_s\mathbf{r}(0) = 0$. The excellent agreement between the theoretical and the measured geometrical parameters plotted in Figure 2 demonstrates that this simplified approach correctly captures the main features of the filament dynamics. Although this linear equation can be solved analytically, the form of the exact solution is so complex that it is not really insightful. We rather detail here the two asymptotic regimes $Sp \sim [L/l(\omega)]^4 \ll 1$ and $Sp \sim [L/l(\omega)]^4 \gg 1$ corresponding to almost straight and tightly wrapped rods respectively. In the limit of large $l(\omega)$ (low speeds), the solution of the two above equations is:

$$r_1 = -\frac{L\tan\theta}{120} Sp \left[20\,(s/L)^2 - (10s/L)^3 + (s/L)^5\right] \quad (4)$$
$$r_2 = \mathcal{O}(\mathrm{Sp}^2)\,. \quad (5)$$

It then follows that the rotation mostly bends the filament in the flow direction, the distance $d(L)$ is thus expected to remain constant at low speed. Conversely, since the filament responds linearly to the viscous flow, the wrapping angle $\phi \sim r_1(L)/(L\sin\theta)$ increases linearly with Sp: $\phi = (11/120)Sp$. These two predictions thus correctly capture the main features of two experimental observations reported in Figure 2. In the limit of small $l(\omega)$ (high speeds), Eqs. 2 and 3 reduce to $r_2(s) = -s\tan\theta$ and $r_1 = 0$. This immediately tells us that the filament is now completely aligned along the rotation axis in this high speed regime. More precisely, the flow induces a strong bending of the filament but the curvature is only localized in a region of length $l(\omega)$ near the anchoring point on the z axis. This explains the surprising collapse seen in our experimental pictures, Figure 2. Our second main objective is now to assess the impact of this rotation-induced wrapping on the (propulsive) axial force F created by the flow and on the torque required to enforce the stationary rotation.

We first focus our attention on the variation of the axial force in an angular velocity-controlled experiment. Our accurate filament detection algorithm enables us to measure axial force $F = \int \mathbf{f}_v(s)\cdot\mathbf{e}_z\, ds$ values as low as $3\,n$N. Contrary to what would be observed with a rigid filament, we systematically measure a non zero axial force. Moreover the direction of the force is independent of the sign of the angular velocity. This can be understood by looking at the symmetry of the deformed filaments. A positive (resp. negative) ω induces left- (resp. right-) handed helical stationary deformations to the initially straight flexible rods. Besides it is well known that a left- (resp. right-) handed chiral object rotating in the clockwise (resp. anticlockwise) direction experiences an upward (resp. downward) viscous force. We can thus anticipate that the axial force F should increase quadratically with ω at least in the low Sp limit. Dimensional analysis then implies that F should scale as $F_\mathrm{e}\mathrm{Sp}^2$, where we define the elastic force $F_\mathrm{e} \equiv \kappa/L^2$. To go beyond this scaling prediction we can compute the total force knowing the filament shape in the low Sp limit thanks to our simplified linear model (Eq. 4):

$$F = \left(1 - \frac{\eta_\parallel}{\eta_\perp}\right)\frac{\sin^2\theta\cos\theta F_\mathrm{e}}{18}\mathrm{Sp}^2 + \mathcal{O}(\mathrm{Sp}^3). \quad (6)$$

This expression is in excellent agreement with our experimental findings for sperm numbers smaller than 10, Figure 4. This figure shows that F continuously increases with the dimensionless angular speed and reveals a second power-law regime in the other asymptotic limit. For $Sp > 10$, the force scales as $F \sim F_e Sp^{1/2}$. We notice that the crossover between the two power-law behaviors occurs in the narrow range of Sp where the filament starts bending towards the z-axis.

Besides, we have shown that the elastic deformations of the filament are localized over a length $l(\omega)$ in the tightly wrapped conformations. Hence, a simple scaling analysis predicts that the axial force experienced by the

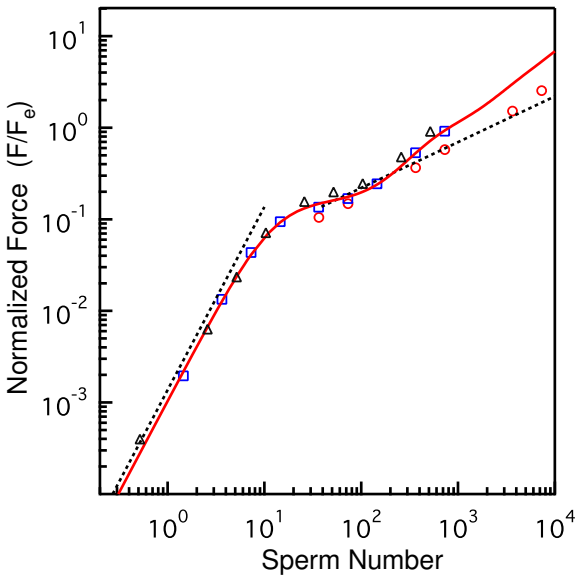

FIG. 4: Propulsive force normalized by the elastic force as a function of Sp for three different filament lengths (triangles: L= 48 mm, squares: L=52.5 mm, circles: L= 96 mm). Dotted lines: Theoretical predictions in the low and high Sp limits given by Eq 6 and ($F/F_e \sim Sp^{1/2}$) respectively. Solid line: Force computed from the profiles obtained by solving Eqs. 2and 3.

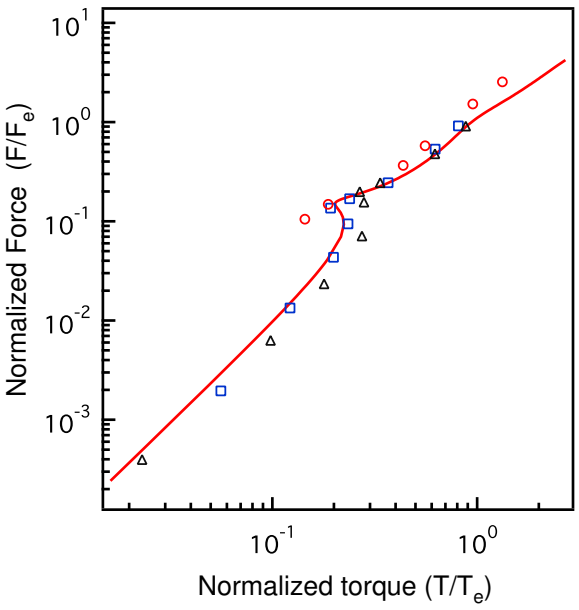

FIG. 5: Normalized propulsive force vs normalized torque for three different filament lengths (triangles: L= 48 mm, squares: L=52.5 mm, circles: L= 96 mm). Solid line: Force-Torque relation obtained according to our linearized model.

filament should scale as $F \sim \eta\omega l^2(\omega)$, or equivalently $F/F_e \sim \mathrm{Sp}^{1/2}$, which is observed in Figure 4.

We now come to our last and important results. We have also systematically computed the viscous torque, T, acting on the flexible rods, from the 3D shape reconstruction: $T = \int [\mathbf{f}_v \cdot \mathbf{e}_z]\, d(s)\mathrm{d}s$, with $d(s)$ the distance from the z axis. In the stationary state the measured viscous torque is equal to the torque delivered by the motor. Hence, we can deduce the evolution of the axial force in a torque-driven experiment from this measured torque. The axial force normalized by the elastic force is plotted versus T/T_e in Figure 5, with the elastic torque $T_e \equiv \kappa/L$. Contrary to what is observed for the force-velocity relation the axial force is a non monotonic function of the applied torque. We stress on the surprising decrease of the force with T for $T \sim 0.2T_e$. This counterintuitive behavior is actually observed for sperm numbers for which the filament collapses on the z axis. A decreasing branch in the torque-force diagram implies that a torque-driven filament would undergo a discontinuous structural transition. This confirms the observations made by Manghi *et al.* in Stokesians numerical simulations [17]. Eventually we also emphasize the remarkable robustness of our simple modeling in accounting for the fluid-structure interaction. This *linear* model yields again an excellent prediction of these strongly *nonlinear* variations of the force with the driving torque (Figure 5).

From a design perspective, the self-induced helicity of an elastic flagellum could be an efficient strategy to drive artificial swimmers. On the one hand, operating at a constant rotational speed ensures a very stable swimming speed. On the other hand, choosing a working point close to the discontinuous shape transition would allow for strong accelerations triggered by a slight variation of the torque command. An interesting issue which goes beyond the scope of this paper deals with the efficiency of such a propulsive mechanism, both in the pumping and the swimming regimes [18].

H. Stone and R. Netz are gratefuly acknowledged for stimulating discussions. We thank N. Champagne, E. Laïk and L. Gani for help with the experiments.

While we were completing this work, we became aware of a very similar study from K. Breuer's group [19].

[1] D. Bray, Cell Movements: From Molecules to Motility, Garland, N.Y. (2001).
[2] S. Camalet, F. Jülicher and J. Prost, *Phys. Rev. Lett* **82** 1590 (1999).
[3] N.Hirokawa, Y. Tanaka,Y.Okada and S.Takeda, *Cell* **125** 33 (2006).
[4] V.N. Manoharan, M.T. Elsesser and D.J. Pine, *Science* **301** 483 (2003)
[5] C. Goubault, P. Jop and M. Fermigier, J. Baudry, E. Bertrand and J. Bibette *Phys. Rev. Lett.* **91** 260802 (2003).
[6] R. Dreyfus, J. Baudry, M. L. Roper, M. Fermigier, H. A. Stone and J. Bibette*Nature* **437** 437 (2005)
[7] A. W. Feinberg, A. Feigel, S.S. Shevkoplyas, S. Sheehy, G. M. Whitesides and K. K. Parker *Science* **317** 1366 (2007)
[8] G. I. Taylor, *Proc. R. Soc. London, Ser. A* **209**, 447 (1951).
[9] E. Lauga, *Phys. Rev E*, **75**, 041916, (2007).
[10] M. Kim, J. C. Bird, A. J. Van Parys, K. S. Breuer and T. R. Powers, *Proc. Natl. Acad. Sci. USA* **100**, 15481 (2003).
[11] C. H. Wiggins, D. Riveline, A. Ott and R. E. Goldstein, Biophys. J. 74, 1043 (1998)
[12] T. S. Yu, E. Lauga and A. E. Hosoi, *Phys. Fluids*, **18**, 091701, 2006
[13] M.Manghi, X. Schlagbergerand and R. Netz, *Phys. Rev . Lett.* **96** 068101 (2006)
[14] A .Vilfan and F. Julicher, *Phys. Rev. Lett.***96**, 058102 (2006).
[15] Chris H. Wiggins and R. E. Goldstein, Phys. Rev. Lett. **80**, 3879 (1998).
[16] G.K. Batchelor, J. Fluid Mech. **44**, 419, (1970)
[17] M. Manghi, X. Schlagberger and R. R. Netz Phys. Rev. Lett. **96** 068101 (2006).
[18] O Raz and J. E. Avron *New J. Phys.* **9** 437 (2007).
[19] C. Qin, T. Powers and K. Breuer submitted to Phys. Rev. Lett. (2008).